Robotics and Autonomous Systems 194 (2025) 105132

Contents lists available at ScienceDirect

Robotics and Autonomous Systems

journal homepage: www.elsevier.com/locate/robot

Circulation-embedded Control Barrier Function for safe navigation: A solution to avoid undesired equilibria and dysfunctional circulation

Shaghayegh Keyumarsi *, Made Widhi Surya Atman [1], Azwirman Gusrialdi

Automation Technology and Mechanical Engineering Unit, Tampere University, Tampere, 33720, Finland

ARTICLE INFO

Keywords:
Control Barrier Function
Deadlocks
Autonomous agents
Collision avoidance

ABSTRACT

The Control Barrier Function (CBF) is widely adopted in safety-critical applications such as safe navigation in an unknown environment. CBF quadratic program (CBF-QP) is a conventional CBF framework that acts as a safety filter. However, CBF-QP is prone to deadlocks, especially in dynamic and multi-agent environments, although it also occurs with convex obstacles. Specifically, CBF-QP suffers from several challenges, including undesired equilibria, accompanying slowdown behavior around these points, dysfunctional circulation, and becoming trapped in the obstacle. In this paper, we propose a practical solution to address these issues. First, we introduce the foundational principles and parameters for the proposed circulation-embedded CBF algorithm, which incorporates an effective circulation linear inequality constraint into CBF-QP. Moreover, input bounds constraints are incorporated to ensure that the rectified input is readily applicable and optimal. Then, we study the feasibility, continuity, equilibrium points, and convergence of the proposed circulation-embedded CBF-QP algorithm through propositions and formal proofs. Finally, the effectiveness of the proposed algorithm is demonstrated through experiments and comparisons involving unknown nonconvex obstacles and multi-robot scenarios without communication. The source code is released for the reference of the community.[2]

1. Introduction

Ensuring the safety of autonomous systems is of utmost importance. CBF [1] has been widely incorporated in safety-critical applications in recent years [2,3]. CBF-QP is a popular framework for completing a robotic task while satisfying CBF constraints, allowing real-time practical implementation. It minimizes the norm of the difference between the reference control input and the rectified control input (the optimization variable) to minimally deviate from the reference control input while meeting the CBF as a linear inequality. Solving this optimization problem ensures safety even if it was overlooked in the control design process for some reason.

Although CBF-QP efficiently ensures safety by solving a QP, it suffers from two main drawbacks: feasibility and potential for deadlocks [2,4]. Specifically, finding the minimizer of the CBF-QP does not guarantee the progression toward the reference control input. CBF deadlocks result in slowed behavior near the undesired equilibrium points introduced by the CBF, or even stabilizing at one of these points in worst-case scenarios. Consequently, safety constraints might hinder the fulfillment of control objectives. These deadlocks arise from two main causes: a small feasibility set and the introduction of CBF undesired equilibria points. Since CBF is a safety filter, if safety measures are not integrated into the reference control design, control objectives may not align with safety requirements. As trajectories are not adequately planned, this misalignment can lead to deadlocks, which are undesired equilibrium points. One common approach to avoid deadlocks is to study the region of attraction of an asymptotically stabilizing control law known to ensure stability and constraint satisfaction. Several works focus on examining the compatibility of Control Lyapunov Functions (CLF) and CBF to achieve this [5–7], limiting the practicality of CBF. The limitation arises from the need for a thorough study of the region of attraction to exclude points where the CBF and control input law are incompatible, thereby shrinking the admissible state space. Following the same line of research, in [8], compatibility and CLF-CBF-QP parameters are analyzed, and a further modification is proposed to remove some of the undesired equilibria that are introduced by coupling CLF and CBF. Meanwhile, the core issue of resolving the potential deadlock problem associated with CBF has recently gained increasing attention. As deadlocks occur less frequently in environments with convex obstacles, Genaro et al. [9] proposed a diffeomorphism-based CBF control strategy

* Corresponding author.
E-mail addresses: shaghayegh.keyumarsi@tuni.fi (S. Keyumarsi), widhi.atman@utu.fi (M.W.S. Atman), azwirman.gusrialdi@tuni.fi (A. Gusrialdi).

[1] At the time of this research, M.W.S. Atman was affiliated with Tampere University. He is now affiliated with the University of Turku.

[2] Code: https://github.com/sh-keyumarsi/Circulation-embedded-CBF.

https://doi.org/10.1016/j.robot.2025.105132
Received 24 October 2024; Received in revised form 23 June 2025; Accepted 16 July 2025
Available online 8 August 2025

for environments with multiple nonconvex obstacles. The diffeomorphism maps the world and obstacles into a ball world where deadlock only happens for a zero-measure set of initial conditions. Two key limitations of this approach are that the obstacle must be known in advance for designing the diffeomorphism maps and that the transformation maps involve mathematical complexity. It is worth mentioning that the deadlock issue of the CBF for convex obstacles can be easily avoided by perturbing the control input [10]. The main limitations of the perturbation method are the persistence of deceleration near deadlocks and the method's ineffectiveness in resolving deadlocks for nonconvex obstacles. Multi-robot deadlock configurations are analyzed in [11], which proposes a symmetry-breaking controller incorporating some random noise based on derived geometric properties, as a resolution. This method requires knowledge of the geometric characteristics of the robot configurations when the system is in deadlock and only addresses multi-robot deadlocks.

In the CBF-QP formulation, the safety is satisfied locally, which could introduce stable undesired equilibrium points. To be more specific, Goncalves et al. in [12] study the vector field generated by CBF and modify the field to explicitly circulate obstacles. In their method, the circulation constraint is gradually activated if the safety function is smaller than a threshold, which occurs when the system is close to the boundary of an obstacle. They proceed by studying the feasibility of the resulting QP, continuity of input, and establishing a weak form of Lyapunov stability. It is worth pointing out that there are no guarantees of successful circulation using this method, i.e., it may result in dysfunctional circulation, especially in the case of nonconvex obstacles. Desai et al. in [13] provide an auxiliary control approach to prevent the system from falling into undesired equilibria. The auxiliary control is activated only when a conflict is identified between the nominal control and the CBF. They leave the selection of the optimal auxiliary control direction for future investigation. Moreover, this method also suffers from dysfunctional circulation. In this work, inspired by the approaches in [12,13], a novel circulation-embedded CBF is proposed that ensures safe navigation in an unknown environment and guarantees convergence to the goal position. In addition, the proposed method also provides a smoother obstacle avoidance maneuver with convergence guarantees by exploring the most effective method of incorporating circulation into the CBF formulation. A comparison with similar previous works is provided in Table 1. Specifically, the contributions of this paper are as follows.

- Elimination of all undesired equilibria and the associated slowing behavior in CBF, resulting in smoother motion and improved obstacle avoidance performance in complex environments.
- The dysfunctional circulation problem in the CBF is addressed through the integration of circulation mechanisms, ensuring successful wall-following when necessary.
- The proposed Circulation-embedded CBF-QP is incorporated with input bounds to enhance practical application.
- The proposed circulation-embedded CBF-QP with input bounds is supported by theoretical guarantees, specifically addressing the feasibility, continuity, and equilibrium points of the proposed circulation-embedded CBF. Furthermore, these results demonstrate convergence.
- The proposed method can be applied to multi-agent deadlocks without requiring communication or any additional knowledge beyond what is already required by CBF. This is in contrast to [11], which focuses solely on multi-agent deadlocks and requires prior knowledge of the robots' configurations.
- We demonstrate the effectiveness of our method in resolving various deadlock scenarios for both single-robot and multi-robot cases through experimental evaluations conducted using on-board LiDAR sensors in an unknown environment.

Table 1
Comparison to prior deadlock resolution works for CBF.

Characteristics\method	CBF-QP	[9]	[10]	[12]	[13]	Our work
Removing all undesired equilibria points	✗	✗	✗	✓	✓	✓
Removing dysfunctional circulation	✗	✓	✗	✗	✗	✓
Removing associated slowdowns	✗	✗	✗	✗	✗	✓
Convergence guarantees	✗	✗	✗	✓	✗	✓
Experiments in unknown environment	✓	✗	✗	✗	✗	✓
Incorporating input bounds	✓	✗	✓	✗	✓	✓

The outline of the paper is as follows. In Section 2, we provide a mathematical notation and an overview of the mathematical foundations utilized in this paper. The problem statement is described in Section 3. The proposed circulation-embedded CBF-QP is thoroughly examined in Section 4, followed by its analysis in Section 5. The experimental results are presented in Section 6, and the concluding remarks are summarized in Section 7.

2. Preliminaries

2.1. Mathematical notation

The set of nonnegative reals is denoted by $\mathbb{R}^+ = \{x \in \mathbb{R} \mid x > 0\}$. Let $\mathbb{U}^n$ be the subset of normalized vectors of size n, i.e. $\mathbb{U} = \{v \in \mathbb{R}^n \mid \|v\| = 1\}$. The state of the system is defined as $x \subset \mathbb{R}^n$. I_n denotes the identity matrix of dimensions $n \times n$. $\mathbf{1}_n$ represents a vector comprising ones and is of size $n \times 1$. The operator $\nabla = \frac{\partial}{\partial x}$ calculates the gradient of a scalar function to x as a row vector. For simplicity and brevity, time dependencies are omitted in equations other than the state space. The set difference is denoted by $A \setminus B$ and includes all elements x that are in A but not in B. The symbol $\angle(\cdot,\cdot)$ denotes the angle between two vectors. The notation 's' refers to the unit of time measured in seconds, whereas 'm' represents the measurement of distance in meters.

2.2. Control barrier functions and induced undesired equilibria

Consider a nonlinear control-affine system $\mathcal{P}$,

$$\dot{x}(t) = f(x(t)) + g(x(t))u(t), \tag{1}$$

where $x \in \mathcal{X} \subseteq \mathbb{R}^2$ is the state of the system and $u \in \mathbb{R}^2$ is the control input. The vector fields f and g are assumed to be continuous, locally Lipschitz, and the origin is an equilibrium point of $\mathcal{P}$. Assume that the state space can be decomposed into a *safe set* $\mathcal{X}_S$ and an *unsafe set* $\mathcal{X}_U$,

$$\mathcal{X}_S = \{x \in \mathcal{X} \mid h(x) \geq 0\}, \tag{2a}$$

$$\mathcal{X}_U = \{x \in \mathcal{X} \mid h(x) < 0\}, \tag{2b}$$

The system remains safe if $\mathcal{X}_S$ is forward invariant. The CBF, defined as follows, gives the necessary and sufficient conditions for forward invariance of $\mathcal{X}_S$.

Definition 1 (*CBF [14]*). Given the dynamic system $\mathcal{P}$ as in (1), the safe set $\mathcal{S}$ which can be modeled as the *super-level set* of a continuously differentiable function $h : \mathbb{R}^2 \to \mathbb{R}$, the function *h(x)* is a CBF, if there exists a locally Lipschitz, extended $class-\kappa_\infty$ function γ (i.e., $\gamma(0) = 0$ and it is strictly increasing) such that for any $x \in \mathcal{X}_S$,

$$\sup_{u \in \mathbb{R}^2} L_f h(x) + L_g h(x) u + \gamma(h(x)) \geq 0. \tag{3}$$

A safe and minimally invasive controller can be calculated based on the admissible control space of the CBF (4). Specifically, the nominal control u_{nom} can be rectified as the control input u using the following QP:

$$u(t) = \underset{u \in \mathbb{R}^2}{\operatorname{argmin}} \ \frac{1}{2} \left\| u - u_{\text{nom}}(t) \right\|^2 \tag{4a}$$

$$\text{Subject to:} \quad L_f h + L_g h u + \gamma(h(x)) \geq 0, \tag{4b}$$

where the Lie derivatives of $h(x)$ along the vector fields f and g are denoted by $L_f h = \nabla h(x) f(x)$ and $L_g h = \nabla h(x) g(x)$ respectively.

The undesirable equilibria in CBF-QP configuration occur due to conflicts between the safety constraints and nominal control objectives. Simply put, it happens when the system approaches regions when the CBF constraint becomes active, resulting in a zero rectified control input (i.e., the solution u(t) in (4) equals zero) while the nominal input (u_{nom}) is still nonzero. This adjustment results in the introduction of new undesired equilibrium points. To demonstrate their existence, the Karush–Kuhn–Tucker (KKT) conditions are applied, which are necessary conditions for a solution to be optimal. To study KKT conditions, the Lagrangian function of CBF-QP in (4) is calculated as follows using the Lagrangian multiplier λ:

$$\mathcal{L}(u, \lambda) = \frac{1}{2} \left\| u - u_{\text{nom}}(t) \right\|^2 - \lambda (L_f h + L_g h u + \gamma(h(x)))$$

The KKT conditions for system (1) and CBF-QP (4) are as follows:

- Stationary condition:

$$\begin{aligned} &\frac{\partial \mathcal{L}}{\partial u} \ni 0 \Rightarrow \\ &u - u_{\text{nom}} - \lambda g^T(x) \nabla h^T(x) \ni 0 \Rightarrow \\ &u = u_{\text{nom}} + \lambda g^T(x) \nabla h^T(x). \end{aligned} \tag{5}$$

- Primal feasibility:

$$L_f h(x) + L_g h(x) u + \gamma(h(x)) \geq 0. \tag{6}$$

- Dual feasibility:

$$\lambda \geq 0. \tag{7}$$

- Complementary slackness:

$$\lambda (L_f h(x) + L_g h(x) u + \gamma(h(x))) = 0. \tag{8}$$

There are two possible cases: the system remains safe with $\lambda = 0$ and the CBF is not activated, resulting in $u = u_{\text{nom}}$, or CBF is activated with $\lambda \neq 0$. In the latter case, using (5) and (8) we can compute λ as,

$$\lambda = \frac{1}{\left\| L_g h \right\|^2} (-L_f h - L_g h u_{\text{nom}} - \gamma(h(x))). \tag{9}$$

According to (5), the rectified control input u deviates from u_{nom} to ensure safety. From (8) and $\lambda \geq 0$, this deviation directly attenuates the rectified control input when $-g^T(x) \nabla h^T(x)$ and u_{nom} are aligned. This attenuation worsens as λ increases, approaching the boundary of the safe set, potentially leading to the creation of undesired equilibrium points.

3. Problem statement

Consider a mobile robot with single-integrator (SI) dynamics,

$$\dot{x}(t) = u(t), \tag{10}$$

where $x(t) \in \mathcal{X} \subseteq \mathbb{R}^2$ is the robot position and $u(t) \subseteq \mathbb{R}^2$ is the velocity input. It is assumed that the input is bounded, i.e., $\|u\| \leq u_{\text{m}}$. The state space may include obstacles and system limitations, defined as the unsafe set $\mathcal{X}_{\mathcal{U}} \subset \mathbb{R}^2$. The unsafe set can comprise multiple 3-dimensional static or dynamic closed sets. The state space can be partitioned into *safe set* $\mathcal{X}_{\mathcal{S}}$ and *unsafe set* $\mathcal{X}_{\mathcal{U}}$ such that $\mathcal{X}_{\mathcal{S}} \cup \mathcal{X}_{\mathcal{U}} = \mathcal{X}$ in each instance. The nominal go-to-goal controller u_{nom} is given at any time and only vanishes once it has achieved a goal position (target state) x_g. The CBF-QP is used as a low-level safety controller to avoid entering $\mathcal{X}_{\mathcal{U}}$ by applying the rectified control input u. As demonstrated in Section 2.2, the standard CBF-QP can induce undesired equilibrium points that can hinder convergence to the goal position. To address this problem, an additional constraint that enforces circulation has been introduced into the original CBF-QP through various approaches. However, the effectiveness of circulation in enabling the system to proceed further needs to be verified. Furthermore, if the undesired equilibria are only targeted as singular points to be resolved, then other complications such as the slowing down behavior that happens near them remain. In this paper, we aim to address the aforementioned issues by identifying the underlying causes of induced undesired equilibria and introducing an effective circulation constraint into CBF-QP with convergence guarantees.

Problem 1. Consider a single integrator (SI) mobile robot (10) navigating in an environment with obstacles. It has a nominal go-to-goal controller to reach a goal position and is equipped with CBF-QP as a safety filter. The objective is to extend the existing CBF-QP framework to remove the potential undesired equilibria induced by CBF and the associated deceleration near these points by incorporating circulation, while also guaranteeing convergence to the goal position.

Remark 1. In spite of its simplicity, the single integrator kinematic model (10) can be effectively used to control mobile robots that follow unicycle models, such as wheeled robots, by utilizing the near-diffeomorphism approach [15] as will be demonstrated in Section 6.1.

4. Main results: Circulation-embedded CBF-QP

We aim to enhance the performance of tracking CBF-QP by ensuring that the robot adheres as closely as possible to the nominal control input and minimally deviates, circulating the obstacle to maintain the ability to follow it later, thus eliminating undesired equilibria and the challenges they introduce.

We begin by introducing the circulation notation as follows. Initially, define $\mathcal{X}_h := \{x \in \mathbb{R}^2 \mid \nabla h(x) \text{ is continuous and nonzero}\}$. Next, for $x \in \mathcal{X}_h$, let us define the normalized vector $N(x) = \frac{\nabla h}{\|\nabla h\|}$. Following that, define function $T : \mathbb{U}^2 \to \mathbb{U}^2$ that generates a normalized tangential vector such that $\forall v \in \mathbb{U}^2 : v^T T(v) = 0$. Next, we define $\mathcal{X}_{\mathcal{T}} := \{x \in \mathcal{X}_h \mid T(N(x)) \text{ is continuous}\}$. Given that $T(N(x))$ is defined in $\mathcal{X}_{\mathcal{T}} \setminus \mathcal{X}_{\mathcal{U}}$, the minimum value of $\|\nabla h\|$ in this set shall be denoted as $l_h \in \mathbb{R}^+$. Finally, Assumption 1 is introduced to enable us to construct and incorporate the circulation inequality.

Assumption 1. The assumptions are as follows:

1. The states of the system remains within the region where circulation can be defined, i.e. $x \in \mathcal{X}_{\mathcal{T}}$. Additionally, the goal position x_g is also located where circulation is defined and lies within the safe set, i.e., $x_g \in \mathcal{X}_{\mathcal{T}} \setminus \mathcal{X}_{\mathcal{U}}$.
2. The set $\mathcal{X}_{\mathcal{T}} \setminus \mathcal{X}_{\mathcal{U}}$ is not empty.
3. The safety function $h(x)$ is a measure of distance to the unsafe set $\mathcal{X}_{\mathcal{U}}$.

It is worth noting that, although it is desirable that the rectified control input be defined in $\mathcal{X}_{\mathcal{S}}$, we require $T(N(x))$ to be well defined and continuous. This facilitates the introduction of circulation into the CBF if necessary.

4.1. Circulation-embedded CBF synthesis

The proposed solution is a Circulation-embedded CBF-QP with input bounds (11) for a SI system, where the circulation is imposed via the inequality (11c), and the linearized bounded input constraint inequality as presented in (11d).

$$u = \underset{u \in \mathbb{R}^m}{\operatorname{argmin}} \ \frac{1}{2} \left\| u - u_{\text{nom}} \right\|^2 \tag{11a}$$

$$\text{Subject to:} \quad \nabla h(x) \cdot u + \gamma(h(x)) \geq 0, \tag{11b}$$

$$u_{\text{cir}}^T \cdot u \geq k_{\text{sts}}(x), \tag{11c}$$

$$\|u\|_\infty \leq \frac{1}{\sqrt{2}} u_{\text{m}}, \tag{11d}$$

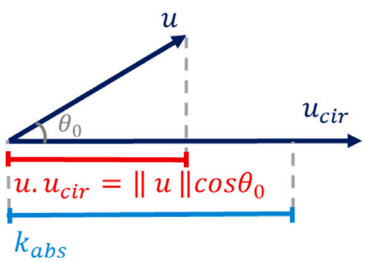

Fig. 1. This figure illustrates how the circulation inequality constraint imposes the control input u to have an image size of k_{abs} in the circulation direction upon activation.

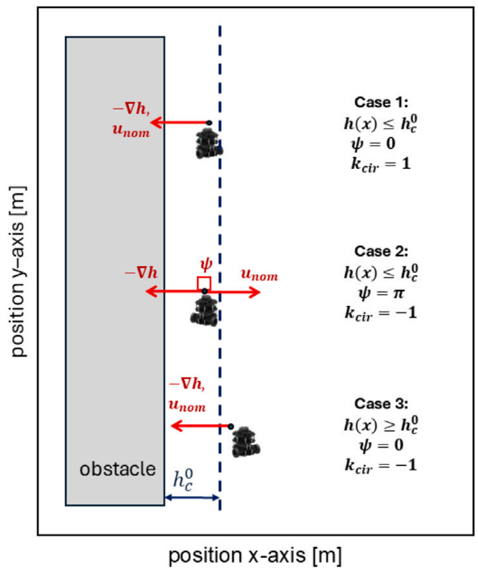

Fig. 2. This figure illustrates the value of k_{cir} for three different cases. Cases 1 and 2 show ψ's role in determining the alignment between the robot's direction with the safety function gradient, while Case 3 illustrates how the proximity threshold h_c^0 determines if circulation is needed.

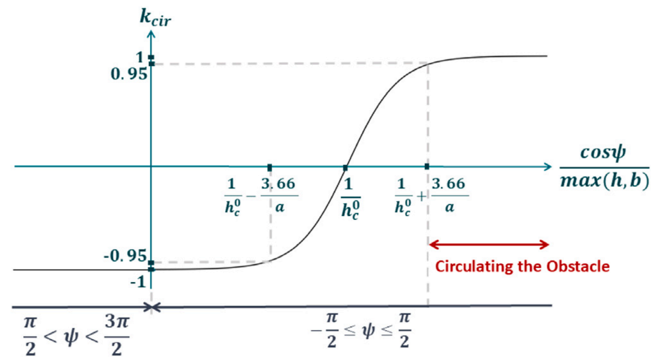

Fig. 3. This figure shows plot of circulation coefficient "k_{cir}" as a function of ψ and $h(x)$. The function's behavior is divided into two primary phases. Note that increasing a steepens the sigmoid curve, while decreasing a flattens it, affecting the sharpness of the transition between −1 and 1.

In (11), $u_{\mathrm{cir}} \in \mathbb{U}^2$ is the normalized direction of circulation, $k_{\mathrm{sts}} \in [-u_{\mathrm{m}}, k_{\mathrm{abs}}]$ is the circulation status coefficient, and $k_{\mathrm{abs}} \in (0, \frac{u_{\mathrm{m}}}{\sqrt{2}}]$ sets the magnitude of control input in circulation direction upon activated. Henceforth, the input-bounded circulation-embedded CBF-QP problem given by (11) will be referred to as *IB-CE-CBFQP*. Next, we will explore the circulation constraint, analyze its behavior, and proceed to design the parameters u_{cir} and k_{sts} in the subsequent subsections. Particularly, this supplementary circulation linear inequality (11c) is based on the notation that it is only activated near undesired equilibrium points. Upon activation, it forces the robot to adhere to the current level set of the safety function, thus removing the unwanted equilibrium. The level set is followed by the requirement that the rectified control input has an image of the norm k_{abs} in the direction of circulation as shown in Fig. 1.

4.2. Circulation coefficient k_{cir}

The following is the proposed coefficient for circulation status, denoted as k_{sts}:

$$k_{\mathrm{sts}}(x) = \frac{1}{2}(k_{\mathrm{abs}} - u_{\mathrm{m}}) + \frac{k_{\mathrm{cir}}(x)}{2}(k_{\mathrm{abs}} + u_{\mathrm{m}}), \tag{12}$$

where $k_{\mathrm{cir}} \in [-1, 1]$ is the circulation coefficient. The primary objective of the design is to guarantee a rapid transition of $k_{\mathrm{cir}}(x)$ from −1 to +1 whenever circulation is necessitated. Furthermore, $k_{\mathrm{sts}}(x)$ effectively maps this interval to the range $-u_{\mathrm{m}}$ to k_{abs}. This specified range represents the states in which the circulation is characterized as either active or inactive with the intended velocity norm bound. $k_{\mathrm{cir}}(x)$ should be designed such that it activates inequality (11c) when the mobile robot approaches a threshold near the boundaries of the safe set, and when $\nabla h(x)g(x)\big|_{SI} = -\nabla h(x)$ (row vector) and u_{nom} are approaching parallel alignment as discussed in Section 2.2. The proximity to the boundary is measured by the inverse of the safety function, $h(x)^{-1}$, which increases as the mobile robot approaches the boundary due to their proportional relationship. Furthermore, to study the collinearity, the angle ψ is defined as,

$$\psi = \angle(-\nabla h(x), u_{\mathrm{nom}}). \tag{13}$$

Hence, the alignment can be determined by calculating $\cos(\psi)$, which captures this feature perfectly by reaching its maximum when collinearity is achieved and turning negative when both vectors point in opposite directions. Progressing with design, we propose the circulation coefficient $k_{\mathrm{cir}}(x)$ utilizing the following sigmoid function,

$$k_{\mathrm{cir}}(x) = 2\left(1 + e^{-a\left(\frac{\cos\psi}{\max(h(x),b)} - \frac{1}{h_c^0}\right)}\right)^{-1} - 1, \tag{14}$$

where ψ is the alignment angle as in (13), $a \in \mathbb{R}^+$ determines the slope of transition, $b \in (0, h_c^0]$, and $0 < h_c^0 < h(x_g)$ is the proximity threshold to the boundary of the safe set to check if circulation is needed. The elucidation of the selection process for all design parameters of $k_{\mathrm{cir}}(x)$ will be discussed at the end of this subsection.

Fig. 2 shows the value of k_{cir} based on $h(x)$ and ψ for three different cases to better illustrate their relationship. Additionally, the plot of k_{cir} designed using the sigmoid function is shown in Fig. 3. As shown in Fig. 3, provided that the angle ψ remains within the range of $\frac{\pi}{2}$ to $\frac{3\pi}{2}$, we obtain $k_{\mathrm{cir}} \approx -1$, thus ensuring that the circulation constraint (11c) remains inactive. Simply put, provided that the mobile robot does not directly approach the boundary of the safe set, it will adopt safe portion of u_{nom} (similar to standard CBF-QP) regardless of its proximity to the boundary. Similarly, u_{nom} is still adopted if the angle ψ is between $-\frac{\pi}{2}$ and $\frac{\pi}{2}$, and value of the safety function h is greater than or equal to the threshold value h_c^0. This indicates safe proximity to the boundary despite being directed toward it. As a result, u_{nom} is still continuously adopted. Note that after reaching the proximity threshold $h \le h_c^0$, the circulation will be activated over a small angular range of ψ rather than at a single point at $\psi = 0$. Let us define the range as $-\psi_1 \le \psi \le \psi_1$. This approach was deliberately chosen as it facilitates a smoother transition and helps mitigate the issue of slowing down.

We will now briefly outline the proposed design process for the circulation coefficient parameters. We begin by choosing the proximity threshold, $0 < h_c^0 < h(x_g)$, as the value of the safety function when the slowing down begins to take effect. The choice of a is based on the sigmoid behavior, as illustrated in Fig. 3. A larger parameter a is preferred so that the sigmoid function achieves a faster transition, causing the circulation inequality constraint to either become active with $k_{sts} \approx k_{abs}$ or remain inactive. To achieve this, select a such that the ratio $\frac{3.66a^{-1}}{(h_c^0)^{-1}} \ll 1$. Next, choose the desired $0 \le \psi_1 < \pi/2$. Finally, select b accordingly,

$$b = \cos\psi_1(\frac{1}{h_c^0} + \frac{3.66}{a})^{-1}. \quad (15)$$

It should be noted that this design guarantees $b \in (0, h_c^0)$.

4.3. Circulation direction u_{cir}

To design our Circulation Direction u_{cir} effectively, we will briefly review the main control architecture and objectives. The control framework consists of the nominal controller and a CBF-based safety filter, which enforces constraints on inputs, states, and safety requirements. This two-level hierarchical control is particularly effective for machine learning-based control, nonlinear control, high-order systems, spacecraft, and other applications, as they often involve relaxation approximations, linearization, or complex computations that benefit from an additional layer of constraint satisfaction or distributed computational load. The rectification of the control input by the CBF should be minimized to adhere closely to the nominal control policy, as deviations may be irreversible or demand substantial corrective input if solely constraint satisfaction is prioritized over minimizing rectification. Returning to the concept of circulation, circulation is triggered when one or more constraints are active, resulting in a nearly zero rectified control input. Thus, by navigating along the boundary of our optimization constraint, we aim to minimally adjust the control input until the nominal input can be resumed. For a more comprehensive discussion on safety filters and the comparison between trajectory planning and CBF, please refer to [16]. In the following subsections, we briefly discuss the proposed approach to derive the circulation direction.

For successful circulation, we require the mobile robot to move along the normalized tangential vector to the border of the unsafe region. Note that the circulation should be designed on the basis of the robot's dynamics to ensure the robot's motion along this tangential vector circulates the boundary of the unsafe region. This can be calculated for an SI mobile robot as follows. A well-defined and continuous function $T(x)$ is defined to get the circulation direction. One way of achieving the tangential vector is by using $\nabla h(x)$, that is,

$$u_{cir}(t) = T(N(x)), \quad (16a)$$

$$T(N(x)) = R(\theta_{cir})\frac{\nabla h(x)}{\|\nabla h(x)\|}, \quad (16b)$$

where $R(\theta_{cir})$ rotates the vector by θ_{cir} Radian. As the direction of $\nabla h(x)$ represents the direction in which the distance to the obstacle increases, rotating it by $\theta_{cir} = \pi/2$ will provide the circulation direction. In a 2D space, there are only two possible directions to circulate around a point or obstacle: clockwise or counterclockwise. To achieve this, we rotate the gradient vector by $\theta_{cir} = \pm\pi/2$ using the dot product with the rotation matrix,

$$R(\theta_{cir}) = \begin{bmatrix} \cos(\theta_{cir}) & -\sin(\theta_{cir}) \\ \sin(\theta_{cir}) & \cos(\theta_{cir}) \end{bmatrix}. \quad (17)$$

Remark 2. Extension of circulation to 3D and higher dimensions is challenging due to the increased complexity of the obstacle surface with $m \ge 2$ dimensions, as some exploration on the surface is necessary. This enables the robot to follow the level set of the safety function around the obstacle surface until it can successfully bypass the obstacle. In dimensions greater than two, a single loop around an obstacle does not ensure exploration. For example, 3d surfaces may contain tunnels, cavities, and overhangs that can trap the robot. Generally speaking, the obstacle surface is $m \le n-1$ dimensional. Additionally, according to the Hairy Ball Theorem, there is no nonvanishing continuous tangent vector field on even-dimensional n-spheres. As a result, determining the circulation direction in higher dimensions requires the use of a path-planning method applied in the reduced space of the obstacle surface.

4.4. Effective circulation vs. Dysfunctional looping

Although the design of the circulation inequality constraint is complete up to this point, further refinement is necessary. While momentarily introducing circulation avoids deadlocks and deceleration of CBF, it is even more crucial that the mobile robot progresses toward task satisfaction. Here, dysfunctional circulation is defined as a situation where circulation is introduced in CBF but fails to enable the mobile robot to proceed further, resulting in an idle loop between tracking CBF and circulation. In Fig. 4, trajectory 1 illustrates dysfunctional circulation between CBF and circulation as an example of such scenarios. In this section, we will focus on creating effective circulation as opposed to dysfunctional circulation. Inspired by the Bug algorithm [17], the circulation coefficient is maintained until the mobile robot successfully navigates past the obstacle once activated. It is enforced by a Boolean variable, $Hold_{k_{cir}}$ to pause updating k_{cir}. This prevents the robot from entering a loop of dysfunctional circulation and go-to-goal. Specifically, the circulation is maintained at the initiation of circulation, which is when $k_{cir} > 1-\epsilon_1$ where ϵ_1 is a small positive value introduced because the circulation coefficient, modeled by a sigmoid function, only approaches but never exactly reaches 1. Navigating past the obstacle is verified by verifying that the current minimum distance to the goal position, $d_g(t) = \|x(t) - x_g\|$, is smaller than the distance at the initiation of circulation d_g^0. This is confirmed by $d_g(t) \le d_g^0 - \epsilon_2$ where ϵ_2 is a small positive value introduced to ensure that the obstacle is fully cleared. In Fig. 4, Trajectory 2 demonstrates effective circulation, allowing the mobile robot to successfully advance toward the goal position.

Algorithm 1 summarizes the real-time implementation of IB-CE-CBFQP.

Algorithm 1 Circulation Embedded CBF

Initialization: Ensure $x(0), x_g \in \mathcal{X}_\mathcal{T} \setminus \mathcal{X}_\mathcal{U}$. Choose the parameters of $k_{cir}(x)$, h_c^0, a, and b in alignment with the guidelines outlined in the concluding paragraph of Section 4.2. Set $Hold_{k_{cir}} = False$, select $k_{abs} \in (0, \frac{u_m}{\sqrt{2}}]$, and set $d_g^0 = 0$ for initialization purposes only; it will be updated when circulation starts. Also, assign small positive values to ϵ_1 and ϵ_2.
Procedure:
1: Calculate $u_{nom}(t)$ and $d_g(t)$ at query point $x_* = x(t)$.
2: **if** $Hold_{k_{cir}} = True$ and $d_g(t) \le d_g^0 - \epsilon_2$ **then**
3: $Hold_{k_{cir}} = False$
4: **end if**
5: **if** $Hold_{k_{cir}} = True$ **then**
6: $k_{cir} = 1$ and determine $k_{sts}(x_*)$ using (12).
7: **else**
8: Determine $k_{cir}(x_*)$ and $k_{sts}(x_*)$ using (14) and (12) respectively.
9: **if** $k_{cir}(x) \ge 1 - \epsilon_1$ **then**
10: Set $Hold_{k_{cir}} = True$ and $d_g^0 = d_g(t)$.
11: **end if**
12: **end if**
13: Determine $u_{cir}(t)$ using (16).
14: Solve (11) to compute the rectified control input, $u(t)$.

5. Analysis of circulation embedded CBF

In this subsection, the feasibility, continuity, and equilibrium points of the proposed IB-CE-CBFQP is discussed. We conclude this subsection by demonstrating convergence using these results.

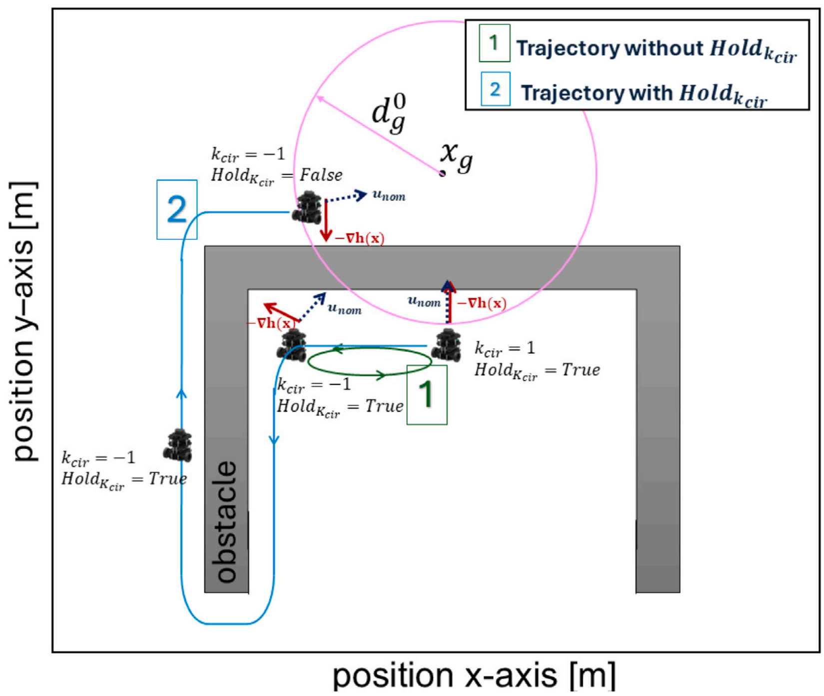

Fig. 4. Trajectories of an SI mobile robot with two different settings. The path labeled 1 represents the trajectory of the robot equipped with the CBF-QP with circulation, highlighting the dysfunctional circulation. The solution of the optimization problem results in dysfunctional circulation because circulation is activated around the undesired equilibrium of CBF, and shortly after moving away from this point, CBF is reactivated solely, leading the system back to the undesired equilibrium point. The path labeled 2 represents the trajectory of the robot equipped with the circulation-embedded CBF-QP, as described in *algorithm* 1, highlighting the effective circulation.

5.1. Feasibility

First, the feasibility of the proposed IB-CE-CBFQP is verified, which serves as the proposed Circulation-Embedded CBF. The feasibility is critical to provide a safe rectified control input u under constraints and system dynamics. Given that we consider SI dynamics, the standard CBF-QP always has at least one feasible solution at $u = 0$. While the overall detailed feasibility of CBF with additional restrictive constraints and/or other system dynamics is beyond the scope of this paper, we focus on the impact of the introduced Circulation-Embedded inequality and input-bounds in the following proposition.

Proposition 1. *The IB-CE-CBFQP, as formulated in (11) with u_{cir} constructed according to (16) and under Assumption 1, is feasible for a SI system.*

Proof. It can be verified as follows that the control input, $u^* = \sqrt{\frac{u_m^2}{2} - k_{\text{abs}}^2}N(x) + k_{\text{abs}}T(N(x))$, satisfies (11b)–(11d) thereby guaranteeing the sustained feasibility of the problem.

I Initially, we establish a lower bound for the safety function value that ensures the robot's safety utilizing the IB-CE-CBFQP method. In this context, we consider the maximum norm of the control input in the $\nabla h(x)$ direction, which consistently meets the conditions specified in (11b)–(11c) which is $u = \sqrt{\frac{u_m^2}{2} - k_{\text{abs}}^2}\nabla h(x) + k_{\text{abs}}T(N(x))$. We also consider $\nabla h(x) = l_h$, so we see the least effect on pushing the robot to the safe set (worst case). Then we find the condition that safety is guaranteed, that is, (11a), is feasible as follows.

$$l_h\sqrt{\frac{u_m^2}{2} - k_{\text{abs}}^2} + \gamma(h(x)) \geq 0. \Rightarrow$$
$$h(x) \geq \gamma^{-1}(-l_h\sqrt{\frac{u_m^2}{2} - k_{\text{abs}}^2}\,). \tag{18}$$

This condition is straightforward to satisfy, as the right-hand side is invariably negative due to $0 < l_h \leq \|\nabla h\|$ and $k_{\text{abs}} \in \left(0, \frac{u_m}{\sqrt{2}}\right]$. Moreover, if the lower bound of $\|\nabla h\|$ is unknown, it is sufficient to confirm $h(x) \geq 0$, a plausible assumption since the robot must be within the safe set to remain safe. Now we use this lower bound to show that the proposed u^* satisfies (11a)as follows.

$$\nabla h(x) \cdot u^* + \gamma(h(x)) \geq \|\nabla h(x)\|\sqrt{\frac{u_m^2}{2} - k_{\text{abs}}^2} - l_h\sqrt{\frac{u_m^2}{2} - k_{\text{abs}}^2} \geq 0.$$

II $u_{\text{cir}}^T \cdot u^* = k_{\text{abs}} \geq k_{\text{sts}}$.

III $\|u^*\|_\infty = \frac{1}{\sqrt{2}}u_{\text{m}}$. □

5.2. Continuity

Subsequently, we demonstrate the continuity of u as a solution of (11).

Proposition 2. *Consider a SI system, under Assumption 1. The control input u, solution to IB-CE-CBFQP (11), with gradually changing k_{sts}, $k_{\ cir}$, and u_{cir} constructed as in (12), (14), and (16), respectively, is a continuous function of x for $x \in \mathcal{X}_T \setminus \mathcal{X}_U$.*

Proof. According to Proposition 2, the problem (11) is feasible, ensuring its regularity, and constitutes a strictly convex quadratic program. Therefore, applying the results in the Continuity of the Solution Map in Quadratic Programming section in [19], we can conclude that the single minimizer u is continuous on the parameters,

$$\left[\begin{matrix} I_2 & -u_{\text{nom}} & \begin{bmatrix} \nabla h \\ T(N(x)) \\ I_2 \\ -I_2 \end{bmatrix} & \begin{bmatrix} \gamma(h) \\ -k_{\text{sts}} \\ -\frac{u_{\text{m}}}{\sqrt{2}}\mathbf{1}_2 \\ -\frac{u_{\text{m}}}{\sqrt{2}}\mathbf{1}_2 \end{bmatrix} \end{matrix}\right]. \quad \square$$

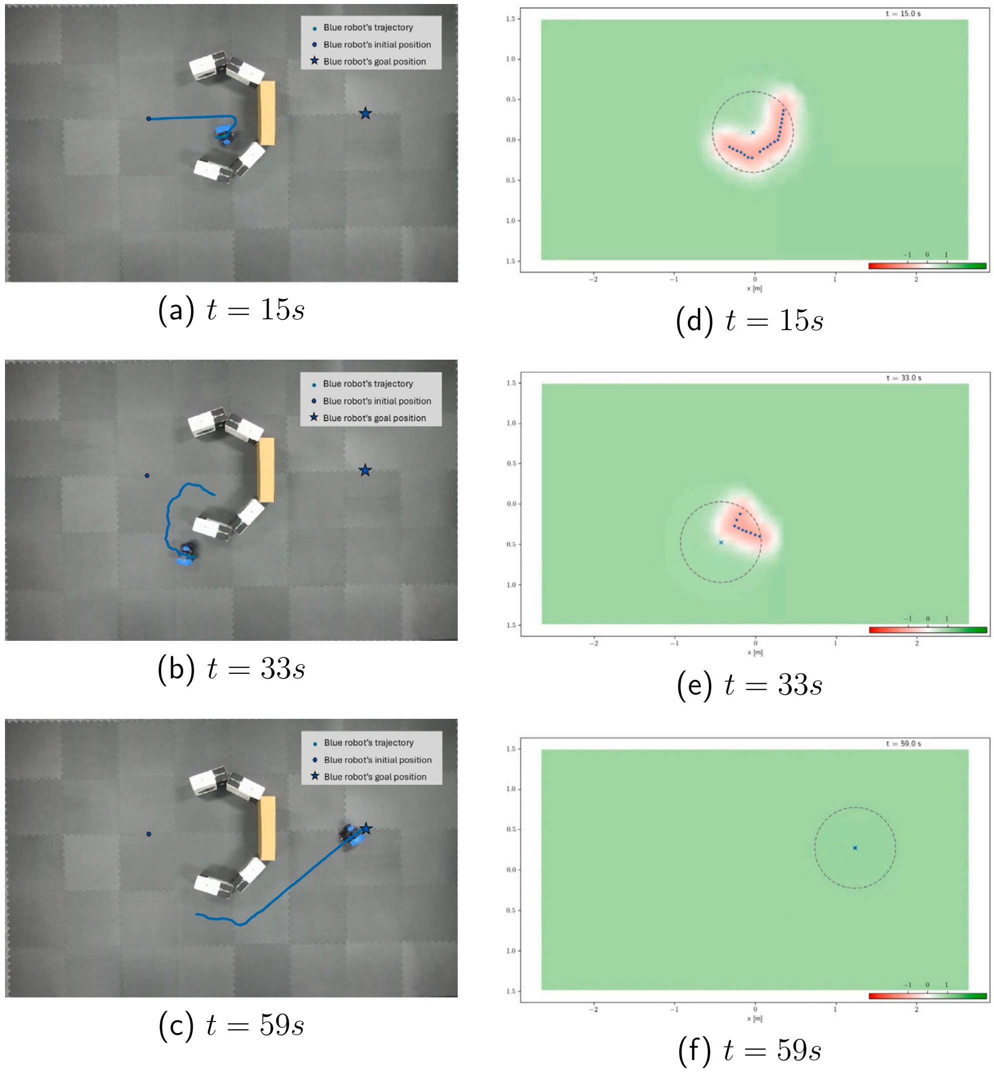

Fig. 5. This figure shows three frames of the implementation instances. The blue colored lines in (a)–(c) depict the trajectory for the TurtleBot equipped with IB-CE-CBFQP as in **Algorithm** 1, while it navigates around a nonconvex obstacle and reaches the goal position. Figures (d)–(f) corresponding to the same time snapshots as (a)–(c), respectively, show the color map plot of the safety function which was leaned online using only LiDAR measurements as in [18] where different colors represent various safety levels. Specifically, green indicates $x \in \mathcal{X}_S$, white represents the borderline safe areas, and red signifies $x \in \mathcal{X}_U$. The video recording of the experiment is accessible at https://youtu.be/69W5bmbBVcI.

5.3. Equilibrium points

Furthermore, the effectiveness of removing the undesired equilibria of CBF is shown in the following theorem.

Theorem 1. *An SI system equipped with a go-to-goal controller and the IB-CE-CBFQP implemented as in algorithm 1 is considered under Assumption 1. The rectified control input u only becomes zero at the goal position.*

Proof. Firstly note that according to Proposition 1, optimization problem (11) is feasible. When $u_{\text{nom}}(x_g) = 0$, $u(x_g) = 0$ stands as the optimal solution for the IB-CE-CBFQP since the cost function equates to zero while adhering to the constraints. Specifically, the input limit is maintained and the circulation remains inactive, considering that according to (14), we have $h_c^0 < h(x_g)$, leading to $k_{\text{sts}} < 0$. Additionally, as stated in Assumption 1, $\gamma(h(x_g)) > 0$ which satisfies the safety constraint (11b).

Assuming $u_{\text{nom}}(x \setminus x_g) \neq 0$ and that $u(x \setminus x_g) = 0$ is a feasible solution, it follows that $\gamma(h(x \setminus x_g)) \geq 0$ and $k_{\text{sts}}(x \setminus x_g) \leq 0$. Also, if $\gamma(h(x \setminus x_g)) \geq 0$, then $h(x \setminus x_g)$ will be nonnegative. Subsequently, we examine all possible scenarios utilizing the KKT conditions, and demonstrate that $u(x \setminus x_g) = 0$ does not represent the optimal solution, thereby concluding the proof. To do so, the Lagrangian function of (11) is calculated as follows using the Lagrangian multiplier λ:

$$\begin{aligned}\mathcal{L}(u,\lambda) = {} & \frac{1}{2}\left\|u - u_{\text{nom}}(t)\right\|^2 - \lambda_1(\nabla h u + \gamma(h)) - \lambda_2(T(N(x))u - k_{\text{sts}}) \\ & + \lambda_3([1\ 0]u - \frac{u_m}{\sqrt{2}}) + \lambda_4([0\ 1]u - \frac{u_m}{\sqrt{2}}) + \lambda_5([-1\ 0]u - \frac{u_m}{\sqrt{2}}) \\ & + \lambda_6([0\ -1]u - \frac{u_m}{\sqrt{2}})\end{aligned} \tag{19}$$

The KKT conditions are then given by:

- Stationary condition:

$$\begin{aligned}& \frac{\partial \mathcal{L}}{\partial u} \ni 0 \Rightarrow \\ & u - u_{\text{nom}} - \lambda_1 \nabla h^T - \lambda_2 T(N(x))^T + \lambda_3[1\ 0] + \lambda_4[0\ 1] \\ & \quad + \lambda_5[-1\ 0] + \lambda_6[0\ -1] \ni 0 \\ & \Rightarrow \\ & u = u_{\text{nom}} + \lambda_1 \nabla h^T + \lambda_2 T(N(x)) - \lambda_3[1\ 0] - \lambda_4[0\ 1] \\ & \quad - \lambda_5[-1\ 0] - \lambda_6[0\ -1].\end{aligned} \tag{20}$$

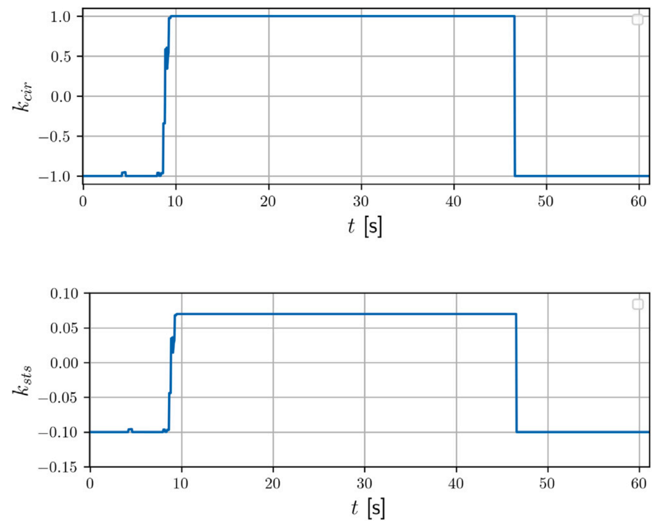

Fig. 6. This figure shows the plot of k_{cir} and k_{sts} over time for the TurtleBot, equipped with IB-CE-CBFQP, as in **Algorithm** 1, while it navigates around a nonconvex obstacle and reaches the goal position. It is evident that k_{sts} effectively maps k_{cir} to the desired range. Note that speed limit $\|u\| \leq 0.1$ m/s; the k_{sts} lower bound is set accordingly, and its upper bound is $k_{\text{abs}} = 0.07$.

- Primal feasibility:

$$\nabla h u + \gamma(h) \geq 0, \tag{21}$$

$$T(N(x))u - k_{\text{sts}} \geq 0, \tag{22}$$

$$\pm I_2 u - \frac{u_m}{\sqrt{2}} \mathbf{1}_2 \leq 0. \tag{23}$$

- Dual feasibility:

$$\lambda_i \geq 0 \text{ for } i = 1, \ldots, 6. \tag{24}$$

- Complementary slackness:

$$\lambda_1(\nabla h u + \gamma(h)) = 0, \tag{25}$$

$$\lambda_2(T(N(x))u - k_{\text{sts}}) = 0, \tag{26}$$

$$\lambda_3([1\ 0]u - \frac{u_m}{\sqrt{2}}) = 0, \tag{27}$$

$$\lambda_4([0\ 1]u - \frac{u_m}{\sqrt{2}}) = 0, \tag{28}$$

$$\lambda_5([-1\ 0]u - \frac{u_m}{\sqrt{2}}) = 0, \tag{29}$$

$$\lambda_6([0\ -1]u - \frac{u_m}{\sqrt{2}}) = 0. \tag{30}$$

According to Eqs. (27)–(30), if any of the Lagrange multipliers λ_i for $i = 3, \ldots, 6$ is non-zero, then (23) holds marginally as a result the control input u is non-zero. Thus, the control input bounds are not active, leading to $\lambda_i = 0$ for $i = 3, \ldots, 6$. Subsequently, we undertake an analysis of the remaining cases:

I $\lambda_i = 0$ for $i = 1, \ldots, 6$**:** Substituting these into (20)yields $u(x \backslash x_g) = u_{\text{nom}}(x \setminus x_g) \neq 0$.

II $\lambda_1 > 0$, and $\lambda_i = 0$ for $i = 2, \ldots, 6$**:** Since $\lambda_2 = 0$, there are two possibilities to consider: according to (14) either $h > h_c^0$ or u_{nom} and $-\nabla h^T$ are not parallel. If $h > h_c^0$, then $\gamma(h) > 0$ will follow. As IB-CE-CBFQP constitutes a Euclidean projection of u_{nom} onto a polyhedron formed by linear inequalities [20] and $u = 0$ fails to satisfy (11b) marginally because $\gamma(h) > 0$, a nonzero optimal solution exists. In the occurrence of the latter scenario, u_{nom} and $-\nabla h^T$ are nonparallel, the control input is the summation of two non-aligned vectors as in (20): $u = u_{\text{nom}} + \lambda_1 \nabla h^T$. As a result, $u_{\text{nom}}(x \setminus x_g) \neq 0$ leads to $u(x \setminus x_g) \neq 0$.

III $\lambda_2 > 0$, and $\lambda_i = 0$ for $i = 1, 3, 4, 5, 6$**:** This situation is deemed impractical because $\lambda_1 = 0$ requires that $h \gg h_c^0$, which subsequently results in (11c) becoming inactive and $\lambda_2 = 0$.

IV $\lambda_1 > 0, \lambda_2 > 0$, and $\lambda_i = 0$ for $i = 3, \ldots, 6$**:** The inequality $\lambda_2 > 0$ requires that $k_{sts} > 0$. if $k_{\text{sts}} > 0$, then $u.u_{\text{cir}} > 0$. As a result, $u \neq 0$ since $u_{\text{cir}} \neq 0$ according to Assumption 1.

It is shown that u attains a value of zero exclusively at the goal position, in concurrence with u_{nom}. As a result, the undesired equilibria are effectively eliminated in IB-CE-CBFQP. □

5.4. Convergence

The following theorem demonstrates that IB-CE-CBFQP effectively addresses Problem 1.

Theorem 2. *An SI system equipped with a go-to-goal controller and IB-CE-CBFQP (11), implemented as in algorithm 1 is considered under Assumption 1. Under these conditions, the mobile robot converges to the goal position.*

Proof. As demonstrated in Propositions 1 and 2, and Theorem 1, IB-CE-CBFQP is both feasible and continuous, with a unique equilibrium point at goal position x_g under the given assumptions. Additionally, the proposed *algorithm* 1 has incorporated circulation that is activated in proximity to undesirable equilibria of CBF and remains until the distance to the obstacle decreases from its initial value at the point of first encounter. This approach ensures that the obstacle is cleared in instances where CBF with circulation alone is insufficient to effectively bypass it. In addition, input-bound constraints are included to verify that the control input adjusted by IB-CE-CBFQP stays secure and feasible to execute, given that all systems feature limited inputs. As a result, the solution of IB-CE-CBFQP can be readily executed to ensure that the mobile robot converges to the goal position. □

6. Experimental validation

In this section, we validate the effectiveness of the proposed IB-CE-CBFQP, as outlined in *algorithm* 1, through experiments. The experimental validation includes three scenarios. First, a single robot navigates in an unknown environment with a nonconvex static obstacle to reach its goal position. Second, we implement the CBF with circulation (without maintaining circulation) for comparison purposes. For the last scenario, four mobile robots, without any communication, navigate toward their goal positions while avoiding collision with other moving robots. The initial and goal positions are chosen so that all robots are trapped in deadlocks under the standard QP-CBF.

6.1. Mobile robot setup, controller design, and circulation-embedded CBF implementation

The TurtleBot3 Burger robot was used as the mobile robot. The dynamics of the TurtleBot can be expressed as:

$$\begin{bmatrix} \dot{p_x}(t) \\ \dot{p_y}(t) \\ \dot{\theta}(t) \end{bmatrix} = \begin{bmatrix} v(t)\cos(\theta(t)) \\ v(t)\sin(\theta(t)) \\ \omega(t) \end{bmatrix}, \tag{31}$$

where p_x and p_y are the position in the x-y plane, $\theta(t)$ is the rotational angle, and the control inputs are the linear velocity $v(t)$ and the angular velocity $\omega(t)$. The control input computed for the SI model in (10) cannot be directly implemented in the Turtlebot3 since it has a nonholonomic constraint, which means it cannot move sideways directly. To address this issue, we apply a near identity diffeomorphism

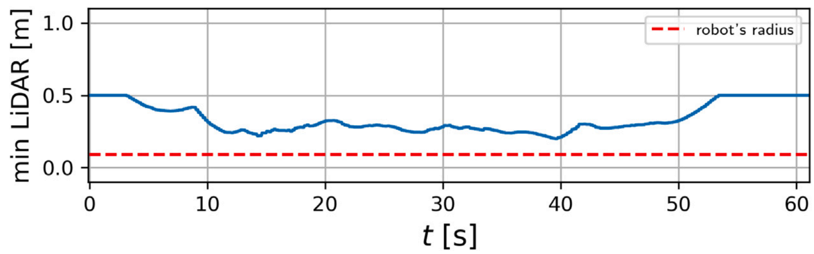

Fig. 7. Plot of the sensed minimum distance to the obstacle by LiDAR over time for the TurtleBot, equipped with IB-CE-CBFQP as in **Algorithm** 1, while it navigates around a nonconvex obstacle and reaches the goal position. The LiDAR maximum detection range is $d_{max} = 0.5$ m, and the red dashed line represents the radius of the TurtleBot.

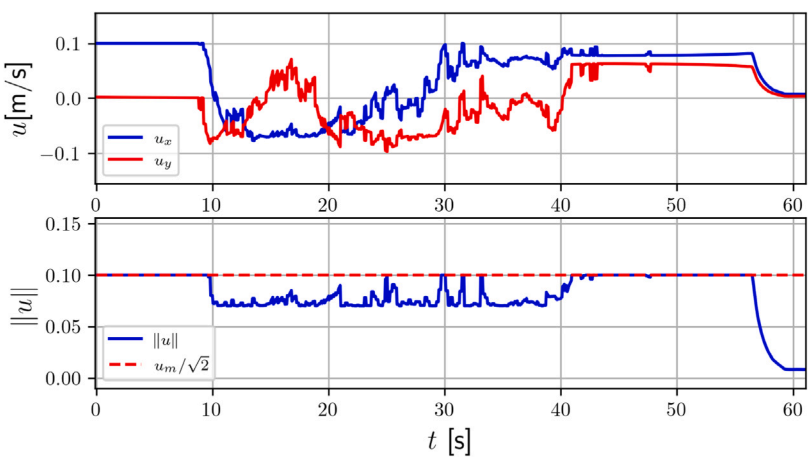

Fig. 8. Plot of the rectified control input u over time for the TurtleBot, equipped with IB-CE-CBFQP as in **Algorithm** 1, while it navigates around a nonconvex obstacle and reaches the goal position. Note that the speed limit $\|u\| \leq 0.1$ m/s is represented by the red dashed line.

transformation [15] that maps the SI input $u(t) = [u_x(t), u_y(t)]^T$ to $v(t)$ and $\omega(t)$. Specifically, $v(t)$ and $\omega(t)$ are given by

$$\begin{bmatrix} v(t) \\ \omega(t) \end{bmatrix} = \begin{bmatrix} \cos(\theta(t)) & sin(\theta(t)) \\ -\frac{1}{l_r} sin(\theta(t)) & \frac{1}{l_r}\cos(\theta(t)) \end{bmatrix} u(t), \tag{32}$$

where $l_r = 0.06$ m is the distance of the controlled point from the middle point between the robot wheels. The $u_{\text{nom}}(t)$ in (11) is designed as a proportional controller, $u_{\text{nom}}(t) = P_{gain}(x_g - x(t))$ with constant gain $P_{gain} = 1$. The experimental setup includes a 5.3 m × 3 m field. The TurtleBot speed limit is set $u_m = 0.1\sqrt{2}$ m/s. The robot position was tracked using a Vicon localization system, and all computations were performed on a remote PC equipped with an Intel i7 processor. The step time is set to 0.02 s. Control inputs were transmitted to the robots via Wi-Fi using ROS messages. The LiDAR data were updated at 5 Hz, with an angular resolution of 1° (360 samples in 2D). The maximum detection range of LiDAR is set as 0.5 m.

To properly establish and operate the circulation, it is crucial that the safety function needs to be smooth and that calculated gradients be dependable. Therefore, a well-designed and robust safety function is fundamental. We propose using the Gaussian Process-derived safety function employing LiDAR sensors as developed in our previous research, [18], to model the CBF safety function in an unknown environment. It is both smooth and robust and includes an integrated noise kernel. This LiDAR-based safety function is efficient in the number of samples and is simple to implement, requiring only basic parameter settings based on the robot radius and maximum velocity to ensure safety. Specifically, by utilizing LiDAR sensor readings, it provides the safety function and its gradient online, which are then used for solving QP-CBF. To be more specific, consider a Gaussian Process-based safety function employing a squared exponential kernel, which is inversely proportional to the reciprocal of Euclidean distance and incorporates a noise kernel for the sampled states x_i and x_j, $k(x_i, x_j) = e^{\frac{-1}{2\ell^2}\|x_i - x_j\|^2} + \sigma^2 I$. The function is characterized by a fixed, positive mean function set to 1, alongside a data set consisting of unsafe positions assigned with the value −1. The safety function is formulated by the average prediction of the modeled Gaussian process (GP). In detail, the hyper-parameters of the LiDAR-based GP safety function are $\ell = 0.18$ for time-varying environments, $\ell = 0.14$ for static environments, and $\sigma = 1e-2$. The minimum sampling distance is $d_{sample} = 0.05$. Furthermore, the function γ in (4) is assigned as $\gamma(h) = h$.

In the context of unstructured or dynamic environments, such as in scenario 3, the safety function is dependent on both time and states. Consequently, the CBF constraint for a single integrator is $\frac{\partial h(x,t)}{\partial x}u + \frac{\partial h(x,t)}{\partial t} + \gamma(h(x,t)) \leq 0$. As demonstrated in [21], To consider an upper boundary on temporal variations of the safety functions and to enhance the robustness in environments with noise, an offset of −0.4 is integrated into the CBF constraint, which is implemented as $\frac{\partial h(x,t)}{\partial x}u + \gamma(h(x,t)) - 0.4 \leq 0$. Moreover, the safety function is updated at each sampling interval, with outdated data being discarded to model $h(x,t)$. This approach allows for the extension of the GP-based CBF to unstructured environments.

For the circulation constraint, the parameters are set as follows: the proximity threshold to the boundary of the safe set is $h_c^0 = 0.8$, the slope of the sigmoid function is $a = 30$, the circulation velocity is $k_{\text{abs}} = 0.7\frac{u_m}{\sqrt{2}}$, $\psi_1 = \frac{\pi}{8}$ radian, and $b = 0.67$.

6.2. Experiment 1: Single robot and nonconvex obstacle avoidance scenario, results, and discussions

In this experiment, a TurtleBot3 robot, equipped with IB-CE-CBFQP as in **Algorithm** 1, navigates towards a goal position after becoming trapped in a nonconvex obstacle.

As illustrated by the trajectory in Figures (a)–(c) of Fig. 5, the robot initially heads towards the goal position. Approximately at $t = 9$ s, the circulation behavior is activated, causing the robot to navigate around

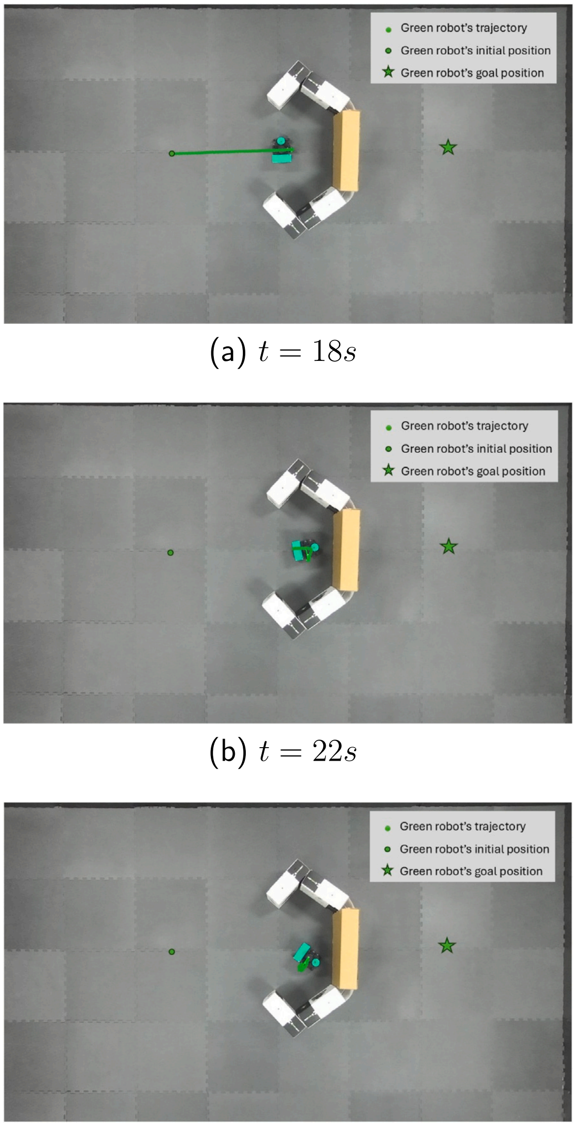

(a) $t = 18s$

(b) $t = 22s$

(c) $t = 48s$

Fig. 9. Three frames of the implementation instances. The green colored lines in (a)–(c) depict the trajectory of the robot equipped with a CBF with circulation (without maintaining the circulation), while it tries to navigate around a nonconvex obstacle and fails to reach the goal position. The video recording of the experiment is accessible at https://youtu.be/69W5bmbBVcI .

the nonconvex obstacle. The circulation approximately continues until $t = 46$ s, where the distance to the goal becomes smaller than the distance at the start of the circulation. Finally, leaving the obstacle behind, the robot reaches the goal position. Figures (d)–(f) of Fig. 5 show the color map of the safety function. Specifically, the 2D space is divided into a grid, and the safety function is computed using a GP model, as described in [18], at each grid point. Subsequently, the local safety function is visualized as a color map, where different colors represent various safety levels. Specifically, green indicates $x \in \mathcal{X}_S$, white represents the borderline safe areas, and red signifies $x \in \mathcal{X}_U$.

Fig. 6 corresponds to the plot of the value of k_{cir} over time. The plot shows the start and end of circulation, which continues until the distance to the goal position becomes smaller than it was at the start of circulation. This approach has successfully enabled the robot to navigate past the nonconvex obstacle. Fig. 7 illustrates the plot of the robot's minimum distance from the obstacle during the experiment over time. It demonstrates that the Circulation-embedded CBF was successful in avoiding collisions. Fig. 8 shows the value and the norm of the rectified control input u by circulation-embedded CBF. It is evident from the figure, no significant deceleration occurs, although a small drop is observed due to the chosen circulation gain $k_{\text{abs}} = 0.07$ m/s.

Remark 3. The TurtleBot3 burger that we used does not respond to very small linear velocity commands at Nebolab (our Laboratory). Specifically, when the input velocity was around 0.01 m/s (1 cm/s) or lower, the robot failed to move. Thus, as observed in the plots of control input over time, the input approaches a value of approximately zero at the goal position.

The experiment demonstrated that the proposed circulation-embedded CBF, **Algorithm** 1, unlike the standard CBF-QP, does not suffer from undesired equilibria at $t \approx 9$ caused by u_{nom} and $-\nabla h^T$ being parallel. Additionally, it is shown that the robot is able to escape from the nonconvex obstacle, unlike scenarios where circulation is momentarily introduced or when only the undesired equilibria location is addressed without considering the overall trajectory as shown in the next experiment.

In the implementation of the solver, the daqp from QPSOLVERS was utilized. Furthermore, for subsequent executions beyond the initial one, the preceding solution served as a warm start. To estimate the runtime of the proposed IB-CE-CBFQP which includes calculating the parameters and solving (11) at each sample time, data collection was conducted : the minimum runtime recorded was 0.000010 s, the maximum runtime was 0.002126 s, and the average runtime was 0.000485 s.

6.3. Experiment 2: Single robot and nonconvex obstacle avoidance without maintaining the circulation scenario, results, and discussions

In this experiment, a TurtleBot3 robot is equipped with a CBF-QP with circulation, i.e., without introducing $Hold_{k_{\text{cir}}}$, and tries to navigate toward a goal position after becoming trapped in a nonconvex obstacle, i.e., dysfunctional looping.

As shown in the trajectory in Fig. 9, the robot initially heads toward the goal position. In Fig. 9 at $t = 18$ s, the circulation behavior is activated, causing the robot to initiate movement in the direction of circulation. Although this activation is shortly engaged and then becomes inactive, it results in an unintended dysfunctional circulation where the robot makes minimal progress toward the goal $t = 48$ s before reversing back in the direction of circulation. In the plot of u over time shown in Fig. 12, the small oscillations between the opposing movements, in the goal direction and the circulation direction, evident in the trajectory, prevent the robot from progressing beyond the nonconvex obstacle. The back-and-forth movement is evident from the repetitive variations in the control corresponding to the activation and deactivation of circulation. Over time, this leads to the robot becoming confined to the same corner where it initially became stuck, as depicted in Fig. 9. This is a form of dysfunctional circulation.

The intermittent activation of circulation behavior is also depicted in the plot of the k_{cir} over time, as shown in Fig. 10. Fig. 11 illustrates the plot of the robot's minimum distance from the obstacle during the experiment over time. Although robot safety is ensured, the CBF-QP with circulation as formulated in (11), similarly to the original CBF-QP approach, prevents the robot from successfully reaching the goal position when navigating around the nonconvex obstacle. Fig. 12 shows the rectified control input u over time. Due to the intermittent activation of the circulation and CBF, the control input drops drastically when the circulation is deactivated, which is consistent with the result shown in the circulation coefficient plot as shown in Fig. 10.

In conclusion, this experiment demonstrated how dysfunctional circulation can prevent the robot from reaching the goal position, a challenge that can occur in CBF-QP without properly managing circulation.

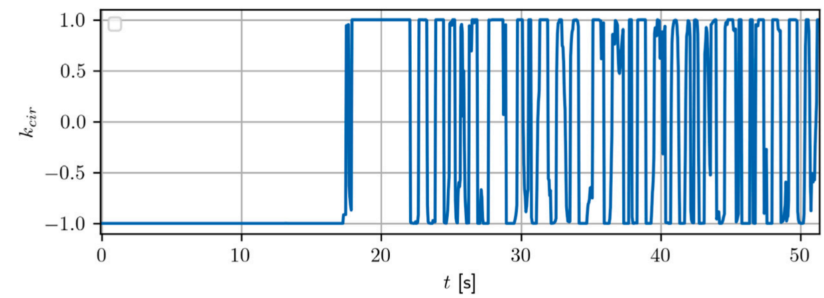

Fig. 10. Plot of k_{cir} over time for the TurtleBot equipped with a CBF with circulation (without maintaining the circulation), while it tries to navigate around a nonconvex obstacle and fails to reach the goal position.

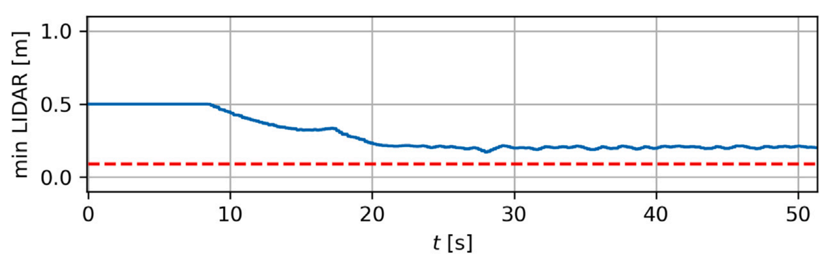

Fig. 11. This figure shows the plot of the sensed minimum distance to the obstacle by LiDAR over time for the Turtlebot equipped with a CBF with circulation (without maintaining the circulation), while it tries to navigate around a nonconvex obstacle and fails to reach the goal position. Note that the LiDAR maximum detection range is $d_{max} = 0.5$ m and the red dashed line represents the radius of the TurtleBot.

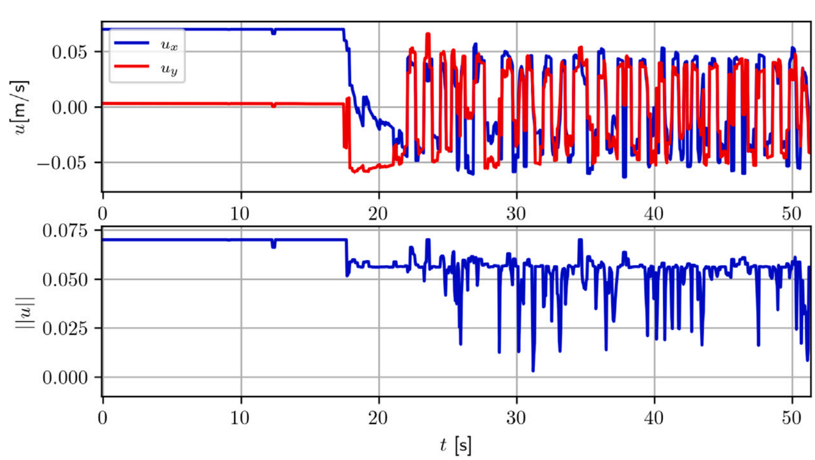

Fig. 12. This figure shows the plot of the rectified control input u over time for the TurtleBot, equipped with a CBF with circulation (without maintaining the circulation), while it tries to navigate around a nonconvex obstacle and fails to reach the goal position. Note that the speed limit $\|u\| \leq 0.07$ m/s.

6.4. Experiment 3: multi-agent deadlock scenario, results, and discussions

In this experiment, four TurtleBot3 robots equipped with IB-CE-CBFQP as in **Algorithm** 1, are placed in a square formation, equidistant from each other. Each TurtleBot's initial position is set at one of the four vertices of the square. The goal of each robot is to navigate to the initial position of the TurtleBot directly in front of it, relying solely on online LiDAR measurements, without any communication between robots or prior knowledge of the environment. The initial and goal positions are selected so that the trajectories will intersect at a central point, creating the potential for a deadlock situation.

The primary objective of this experiment is to investigate how the robots manage to avoid deadlock scenarios at undesired equilibria of CBF-QP and successfully reach their goal positions. As depicted in Fig. 13, the TurtleBots encounter a potential deadlock in the central location. However, due to the activation of the circulation-embedded CBF, the deadlock is successfully resolved. The robots simultaneously begin to circulate around the central point, maintaining smooth trajectories. Once the circulation mechanism has sufficiently resolved the deadlock, the circulation coefficient will be −1, and circulation is deactivated. Then TurtleBots can proceed further.

Fig. 14 corresponds to the plot of the value of k_{cir} of robots over time. Note that obstacles (other robots) are moving. As a result, the

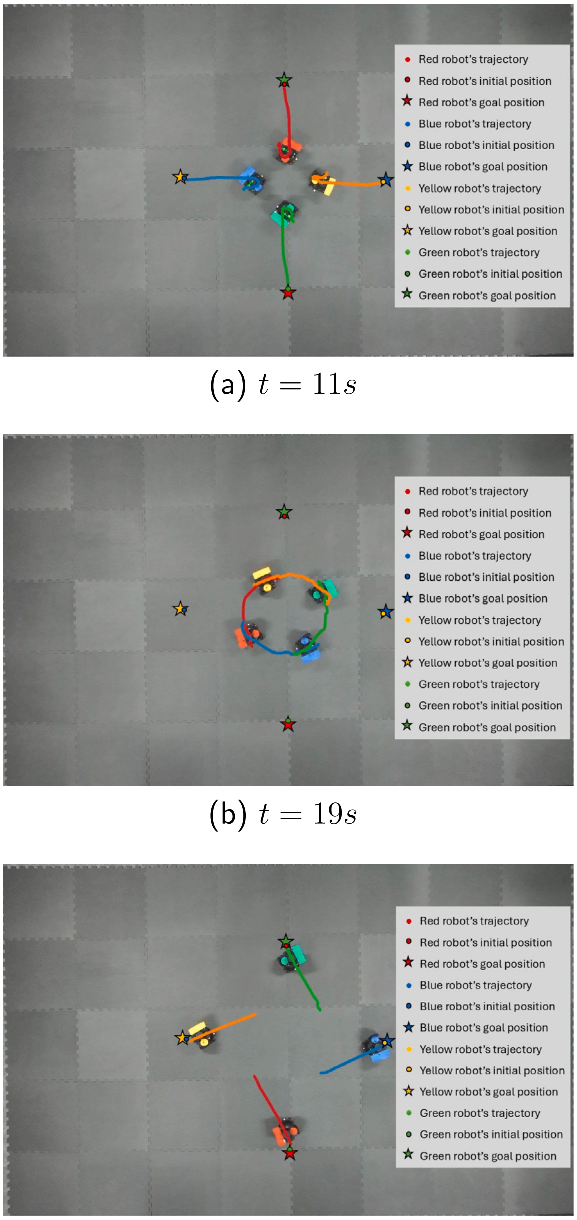

(a) $t = 11s$

(b) $t = 19s$

(c) $t = 27s$

Fig. 13. This figure shows three frames of the implementation instances. The colored lines matching each robot's respective tag color in (a)–(c) show the trajectories of the robots equipped with IB-CE-CBFQP as in **Algorithm** 1, between each snapshot as they get intertwined in a deadlock situation and find their way to their goal positions. The video recording of the experiment is accessible at https://youtu.be/69W5bmbBVcI .

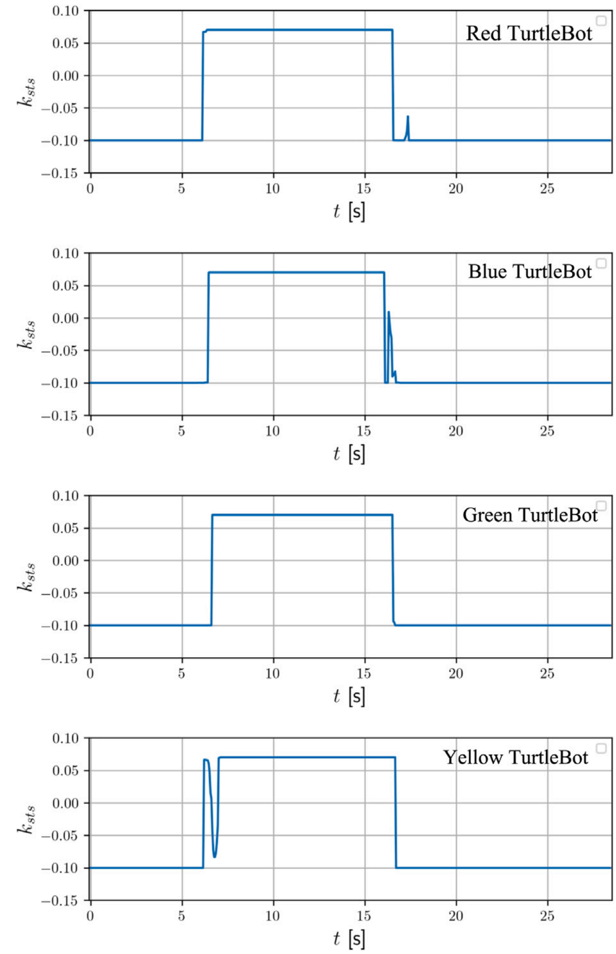

Fig. 14. This figure shows the plots of the value of k_{sts} over time for the TurtleBots equipped with IB-CE-CBFQP as in Algorithm 1 while they get intertwined in a deadlock situation and find their way to their goal positions. Note that speed limit $\|u\| \leq 0.1$ m/s; the k_{sts} lower bound is set accordingly, and its upper bound is $k_{\text{abs}} = 0.07$.

circulation coefficient has little variation, but they simultaneously keep the circulation until they reach a position where the deadlock is resolved. Fig. 15 illustrates the plot of the robot's minimum distance from the obstacle during the experiment over time. It demonstrates that the IB-CE-CBF-QP was successful in avoiding collisions. Fig. 16 shows the value and the norm of the rectified control input u by circulation-embedded CBF. The figure clearly shows that, no significant deceleration occurs, although a small drop is observed due to the chosen proportional gain $k_{\text{abs}} = 0.07$ m/s.

In conclusion, the TurtleBots successfully navigate toward their respective goal positions resolving the deadlock situation. It is also noteworthy that the circulation was maintained relatively consistently during the experiment. Additionally, the LiDAR-based GP safety function, by simply providing the safety function solely based on real-time LiDAR measurement with circulation-embedded CBF enabled the robots to successfully navigate in the unknown environment and resolve the deadlock situation without any communication.

7. Conclusion

In this paper, we present the IB-CE-CBFQP as an extension to CBF-QP for smooth and successful obstacle avoidance. Our approach addresses the challenges of potential undesired equilibria, the common issue of slowing down near obstacles, and dysfunctional circulation by introducing a smooth circulation linear inequality to CBF-QP when necessary. The proposed IB-CE-CBFQP integrates input constraints, crucial for practical CBF implementations. Furthermore, it maintains continuous circulation, rather than on-and-off behavior, contributing to smoother trajectories, effective circulation, and more stable control input for the robot. We supported our findings with theoretical feasibility, continuity, and convergence proofs. Additionally, We demonstrated its success through experimental results and comparison for nonconvex obstacles and for scenarios involving multi-agent deadlock without communication.

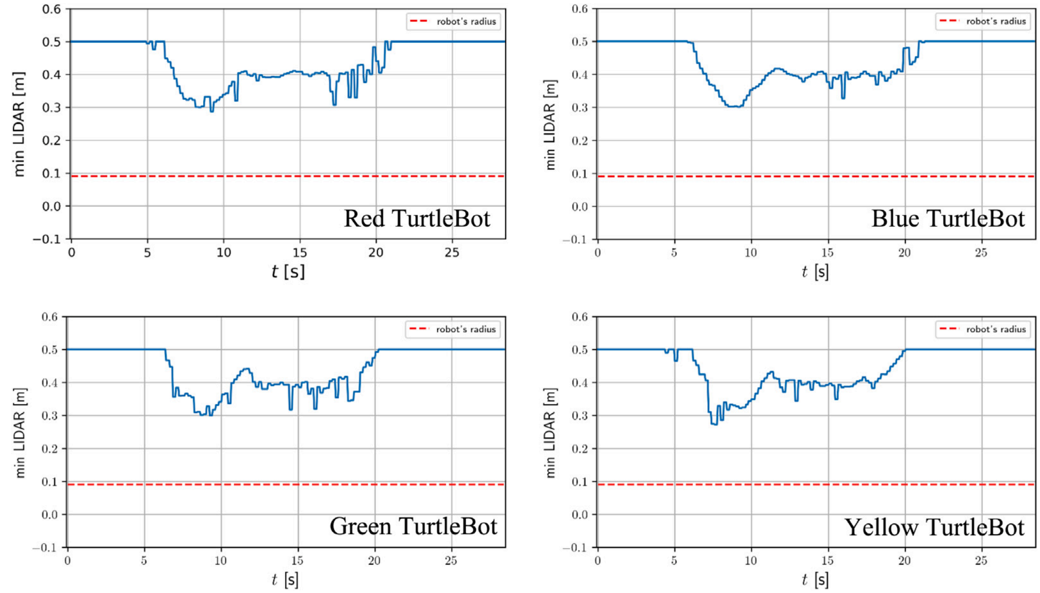

Fig. 15. This figure shows the plot of the sensed minimum distance to the obstacle by LiDAR over time for the TurtleBots equipped with IB-CE-CBFQP as in Algorithm 1 while they get intertwined in a deadlock situation and find their way to their goal positions. Note that the LiDAR maximum detection range is d_{max} = 0.5 m and the red dashed line represents the radius of the TurtleBot.

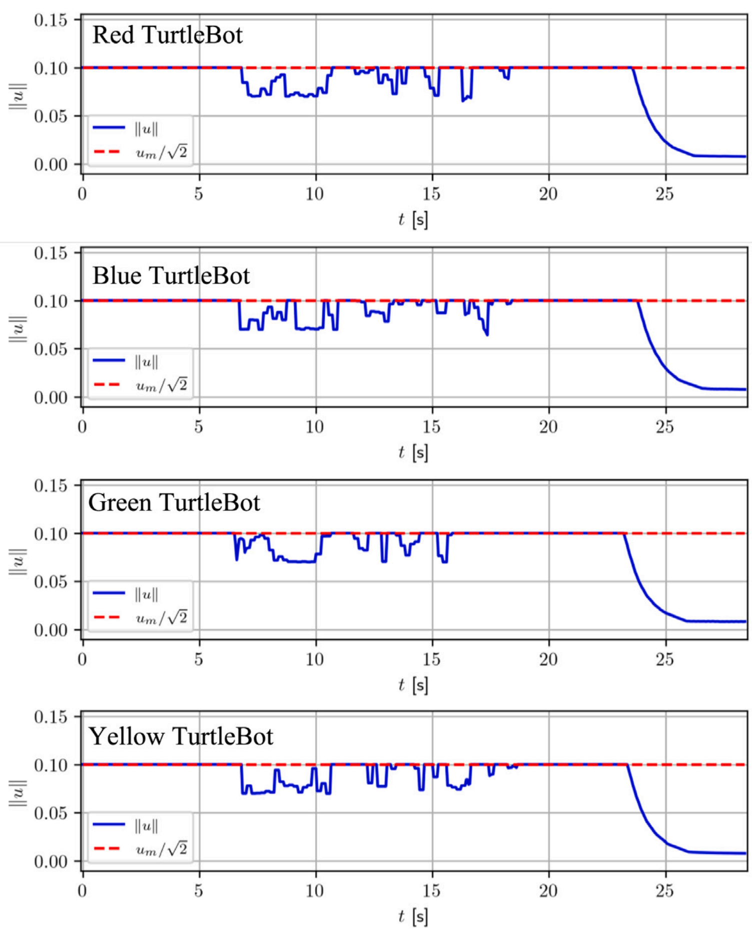

Fig. 16. This figure shows the plot of the rectified control input u over time for the TurtleBots equipped with IB-CE-CBFQP as in Algorithm 1 while they get intertwined in a deadlock situation and find their way to their goal positions. Note that the speed limit $\|u\| \leq 0.1$ m/s is represented by the red dashed line.

CRediT authorship contribution statement

Shaghayegh Keyumarsi: Writing – review & editing, Writing – original draft, Visualization, Validation, Software, Project administration, Methodology, Investigation, Conceptualization. **Made Widhi Surya Atman:** Writing – review & editing, Visualization, Software. **Azwirman Gusrialdi:** Writing – review & editing, Supervision.

Declaration of competing interest

The authors declare that they have no known competing financial interests or personal relationships that could have appeared to influence the work reported in this paper.

Appendix A. Supplementary data

Supplementary material related to this article can be found online at https://doi.org/10.1016/j.robot.2025.105132.

The paper reports real-world experiments; a simulation implementation that reproduces those experiments (source code and generated data) is available at https://github.com/sh-keyumarsi/Circulation-embedded-CBF.

Data availability

No data was used for the research described in the article.

References

[1] A.D. Ames, X. Xu, J.W. Grizzle, P. Tabuada, Control barrier function based quadratic programs for safety critical systems, IEEE Trans. Autom. Control 62 (8) (2017) 3861–3876.
[2] M. Egerstedt, Robot Ecology: Constraint-Based Design for Long-Duration Autonomy, Princeton University Press, 2021.
[3] H. Pham, N. Ranasinghe, D. Le, M.W.S. Atman, A. Gusrialdi, Safety-guaranteed distributed formation control of multi-robot systems over graphs with rigid and elastic edges, IEEE Robot. Autom. Lett. 9 (11) (2024) 10240–10247, http://dx.doi.org/10.1109/LRA.2024.3471460.
[4] M.F. Reis, A.P. Aguiar, P. Tabuada, Control barrier function-based quadratic programs introduce undesirable asymptotically stable equilibria, IEEE Control. Syst. Lett. 5 (2) (2021) 731–736, http://dx.doi.org/10.1109/LCSYS.2020.3004797.
[5] W.S. Cortez, D.V. Dimarogonas, On compatibility and region of attraction for safe, stabilizing control laws, IEEE Trans. Autom. Control 67 (9) (2022) 4924–4931.
[6] P. Mestres, J. Cortes, Optimization-based safe stabilizing feedback with guaranteed region of attraction, IEEE Control. Syst. Lett. 7 (2023) 367–372, http://dx.doi.org/10.1109/LCSYS.2022.3188934.
[7] M.F. Reis, A.P. Aguiar, On the stability of undesirable equilibria in the quadratic program framework for safety-critical control, 2024, http://dx.doi.org/10.48550/arXiv.2402.08027.
[8] X. Tan, D.V. Dimarogonas, On the undesired equilibria induced by control barrier function based quadratic programs, Automatica 159 (2024) 111359, http://dx.doi.org/10.1016/j.automatica.2023.111359.
[9] G. Notomista, M. Saveriano, Safety of dynamical systems with multiple non-convex unsafe sets using control barrier functions, IEEE Control. Syst. Lett. 6 (2022) 1136–1141, http://dx.doi.org/10.1109/LCSYS.2021.3089097.
[10] T. Hu, L. Long, Deadlock avoidance and solution time optimization for discrete-time control systems via control barrier functions, in: 2021 40th Chinese Control Conference, CCC, IEEE, Shanghai, China, 2021, pp. 639–644, http://dx.doi.org/10.23919/CCC52363.2021.9549772.
[11] J. Grover, C. Liu, K. Sycara, The before, during, and after of multi-robot deadlock, Int. J. Robot. Res. 42 (6) (2023) 317–336.
[12] V.M. Gonçalves, P. Krishnamurthy, A. Tzes, F. Khorrami, Control barrier functions with circulation inequalities, IEEE Trans. Control Syst. Technol. (2024) 1–16, http://dx.doi.org/10.1109/TCST.2024.3372802.
[13] M. Desai, A. Ghaffari, Auxiliary control to avoid undesirable equilibria in constrained quadratic programs for trajectory tracking applications, IEEE Trans. Robot. 39 (3) (2023) 2078–2092, http://dx.doi.org/10.1109/TRO.2022.3233346.
[14] A.D. Ames, S. Coogan, M. Egerstedt, G. Notomista, K. Sreenath, P. Tabuada, Control barrier functions: Theory and applications, in: 2019 18th European Control Conference, 2019, pp. 3420–3431.
[15] S. Wilson, P. Glotfelter, L. Wang, S. Mayya, G. Notomista, M. Mote, M. Egerstedt, The robotarium: Globally impactful opportunities, challenges, and lessons learned in remote-access, distributed control of multirobot systems, IEEE Control Syst. Mag. 40 (1) (2020) 26–44.
[16] J. Breeden, Constrained Control and Online Safety Filtering for Autonomous Space Systems (Ph.D. thesis), University of Michigan, 2024.
[17] N. Buniyamin, W.W. Ngah, N. Sariff, Z. Mohamad, et al., A simple local path planning algorithm for autonomous mobile robots, Int. J. Syst. Appl. Eng. Dev. 5 (2) (2011) 151–159.
[18] S. Keyumarsi, M.W.S. Atman, A. Gusrialdi, LiDAR-based online control barrier function synthesis for safe navigation in unknown environments, IEEE Robot. Autom. Lett. 9 (2) (2024) 1043–1050.
[19] G.M. Lee, N.N. Tam, N.D. Yen, Quadratic Programming and Affine Variational Inequalities: a Qualitative Study, vol. 78, Springer Science & Business Media, 2005.
[20] S.P. Boyd, L. Vandenberghe, Convex Optimization, Cambridge University Press, 2004.
[21] K. Garg, D. Panagou, Robust control barrier and control Lyapunov functions with fixed-time convergence guarantees, in: 2021 American Control Conference, ACC, IEEE, 2021, pp. 2292–2297.

Shaghayegh Keyumarsi received her M.Sc. degree in Electrical Engineering, specializing in Control, from Sharif University of Technology, Iran, in 2019. She is currently pursuing her D.Sc. (Tech.) in Automation Science and Engineering at Tampere University, Finland. Her research focuses on safety-critical control for autonomous systems, with applications to mobile machines. Her broader research interests include control theory, machine learning, optimization, and networked cyber-physical systems, with applications in robotics.

Made Widhi Surya Atman received the D.Eng. degree in systems and control engineering from the Tokyo Institute of Technology, in 2020. He was a Postdoctoral Research Fellow at the Automation Technology and Mechanical Engineering, Tampere University, Finland. Since September 2024, he has been a Postdoctoral Researcher at Turku Intelligent Embedded and Robotic Systems, University of Turku, Finland. His research interests include human-swarm interaction, passivity-based control, and distributed optimization and control of networked systems, with application to robotic network and persistent environmental monitoring.

Azwirman Gusrialdi received the Dr.-Ing. degree in control engineering from Technische Universität München, Germany, in 2012. He was a Postdoctoral Researcher at the University of Central Florida, and then joined Tampere University in Finland as a Tenure-Track Assistant Professor in May 2019. He is currently an Associate Professor with the Automation Technology and Mechanical Engineering Unit, and leading the Intelligent Networked Systems Group. His research interests include the design of resilient networked systems, cooperative control, and distributed optimization for networked cyber–physical systems with applications to power systems, intelligent transportation systems, and robotic network.